fractal and fractional

MDPI

Article

Fractal Analysis of Particle Size and Morphology in Single-Particle Breakage Based on 3D Images

Ruidong Li [1], Xiang Gao [1], Shao-Heng He [1,*], Dongheng Ru [2] and Zhi Ding [3]

[1] Department of Civil and Environmental Engineering, The Hong Kong Polytechnic University, Hong Kong, China; 22072096r@connect.polyu.hk (R.L.); xiang.gao@connect.polyu.hk (X.G.)
[2] School of Aerospace Engineering and Applied Mechanics, Tongji University, Shanghai 200092, China; rudongheng@tongji.edu.cn
[3] Department of Civil Engineering, Hangzhou City University, Hangzhou 310015, China; dingz@zucc.edu.cn
* Correspondence: shaoheng.he@polyu.edu.hk

Abstract: The accurate modeling of single-particle breakage based on three-dimensional (3D) images is crucial for understanding the particle-level mechanics of granular materials. This study aims to propose a systematic framework incorporating single-particle breakage experiments and numerical simulations based on a novel 3D particle reconstruction technique for fractal analysis of particle size and morphology in single-particle breakage. First, the vision foundation model is used to generate accurate particles from 3D images. The numerical approach is validated by simulating the single-particle breakage test with multiple Fujian sand particles. Then, the breakage processes of reconstructed sand particles under axial compression are numerically modeled. The relationship between 3D fractal dimensions and particle size, particle crushing strength, and morphology is meticulously investigated. Furthermore, the implications of these relationships on the particle breakage processes are thoroughly discussed, shedding light on the underlying mechanisms that govern particle breakage. The framework offers an effective way to investigate the breakage behavior of single sand particles, which will enhance understanding of the mechanism of the whole particle breakage process.

Keywords: fractal dimension; 3D μCT images; vision foundation models; particle breakage; numerical simulation

Citation: Li, R.; Gao, X.; He, S.-H.; Ru, D.; Ding, Z. Fractal Analysis of Particle Size and Morphology in Single-Particle Breakage Based on 3D Images. *Fractal Fract.* **2024**, *8*, 614. https://doi.org/10.3390/fractalfract8110614

Academic Editor: Alex Elías-Zúñiga

Received: 23 August 2024
Revised: 5 October 2024
Accepted: 16 October 2024
Published: 22 October 2024

1. Introduction

Particle breakage is an extremely important phenomenon in nature, industrial processes, and geotechnical engineering. For example, particle breakage extensively exists in soils and exerts a significant influence on soil behavior by changing soil microstructure [1,2]. The interplay between particle breakage and soil response is critical, dictating the need for a nuanced understanding to ensure the resilience and performance of geotechnical structures. Furthermore, optimizing the percentage of particle breakage during ball milling can effectively increase economic benefits. Therefore, the ability to predict particle breakage in nature or industrial processes has sparked great interest in soil/rock mechanics but has also been a persistent challenge. The mechanism of particle breakage is still poorly understood. Complicated interactions among the contributions of the mineral composition, stress condition, loading rate, particle morphology, and particle distribution will affect or even lead to particle breakage [3,4]. The most efficient way to investigate particle breakage is to conduct single-particle breakage loading tests [5,6]. Single-particle breakage loading tests have been demonstrated to be effective in analyzing energy utilization in comminution processes and material mechanical responses under different stresses, as well as the effect of particle size, morphology, and physical properties on the breakage characteristics [7–9].

Apart from experiments, numerical simulations such as the discrete element method (DEM) have been widely used in investing particle breakage [10,11]. Compared to experi-

mental investigations, numerical simulations are more flexible, supporting the visualization of microscopic characteristics, e.g., the interior fractures. Generally, there are two prevalent approaches utilized in the DEM for breakage simulations. The first one is based on the premise that parent particles are composed of distinct, bonded, and completely resolved child particles from the beginning of the simulation [12,13]. The alternative way, called particle replacement, refers to ways where particles are replaced with child particles, such as spheres and superquadrics. Once the specific failure threshold is reached, those child particles will occupy the geometric space of the parent particle to mimic particle breakage [14,15]. The evolution of grading, anisotropy, energy dissipation, and plastic change during single-particle breakage have been investigated by the DEM widely [15,16]. The effect of particle morphology on single-particle breakage is also well summarized and validated [17,18]. However, most existing studies focus on particles with controlled shapes instead of realistic morphology. The accurate and reliable modeling of the breakage process based on single-particle breakage experiments and three-dimensional (3D) μCT images remains scarce.

In recent years, fractal geometry techniques have found widespread applications in many fields, including medicine, material science, geography, etc. Relatively, there have been a few cases of the application of fractal geometry in geotechnical engineering, especially for single-particle breakage. Research has indicated that the fragmentation of granular materials can be described by a fractal dimension [19]. Arasan et al. analyzed the relationship between the fractal dimension and shape properties of particles but only in two-dimensional (2D) fractals [20]. The investigation of 3D fractal dimensions for single-particle breakage is still unclear, especially for scenarios that combine experiments and numerical simulations. Furthermore, there is currently no comprehensive research examining the effect of particle size and morphology on 3D fractal dimensions.

To this end, this study explores the relationship between fractal dimension and particle size and morphology in single-particle breakage from in experiments to numerical simulations based on 3D images. A novel 3D particle reconstruction technique is proposed and used to obtain the particle morphologies. Furthermore, a series of single-particle loading tests are conducted to investigate the mechanical behaviors of Fujian sand particles selected from the sample for reconstruction. Subsequently, the DEM model is established and calibrated based on experimental results. Finally, a series of numerical simulations are conducted to explore and analyze the relationship between fractal dimensions and particle size and morphology.

2. Materials and Methods

2.1. Materials and Equipment

The Tiniusolsen 50ST multi-parameter testing machine was used for conducting the single-particle crushing tests, as shown in Figure 1a. A variety of load cells are available for differing test materials and methods, providing precise applied load measurements. A compression loading cell was employed to crush the particle that was placed between two load plates, and the loading measuring capacity of the compression loading cell was 5 kN, with a resolution of 0.01 N. During the tests, the displacement ratio of 0.1 mm/min was used until the final fracture of the testing particle occurred, and the corresponding force and displacement were measured for further analysis [21].

The tested material was Fujian sand, known as the Chinese standard sand, which is widely employed in soil mechanics research. It is characterized by a predominant quartz composition that imparts high intrinsic strength to the material. Furthermore, the stable distribution in particle size, shape, and inter-flaw of this material ensures that experimental results are reproducible. In this study, 30 single-particle crushing tests were conducted for the statistical analysis of the fragmentation properties, and the origin-tested sand particles were randomly selected from the following sample used for CT scanning and reconstruction, as shown in Figure 1b. The particle size range used in the crushing test was from 1.2 mm to 2.0 mm, and the average particle size was 1.57 mm.

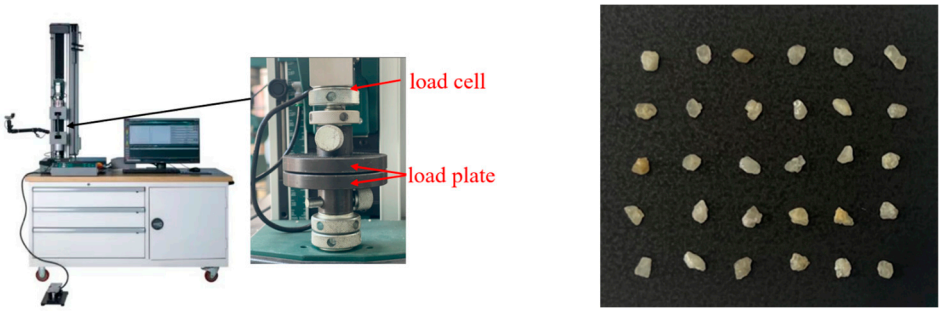

(**a**) (**b**)

Figure 1. Illustrations of experiment: (**a**) loading apparatus; (**b**) tested sand particles.

2.2. Particle Crushing Strength

Tensile failure is considered the primary cause of particle breakage, and a characteristic particle crushing strength derived from the tensile stress defined by Jaeger was employed to analyze the experiment results [22]:

$$\sigma = \frac{F}{d^2} \tag{1}$$

where d is the particle diameter and F is the force applied on the tested particle, measured by the testing machine. In this study, the catastrophic splitting fracture is focused, and the corresponding peak force F_f is employed in the particle strength analysis:

$$\sigma_f = \frac{F_f}{d^2} \tag{2}$$

where σ_f is the particle crushing strength. Therefore, the probability of the survival of a particle at a given stress level σ_c is defined as P_s:

$$P_s = \frac{N\left|\sigma_f \geq \sigma_c\right.}{N_t} \tag{3}$$

where N_t is the total number of particles; $N \mid \sigma_f \geq \sigma_c$ represents the number of particles whose strength σ_f is greater than the given stress σ_c. P_s can be estimated by the Weibull distribution [23]:

$$P_s = \exp[-(\frac{\sigma_f}{\sigma_0})^m] \tag{4}$$

where m is the Weibull modulus and σ_0 is the characteristic stress of the particles, at such a stress level that 37% of the tested particles survived.

2.3. 3D Particle Reconstruction

The Nikon XT H225ST 2X µCT system was used to capture the microstructure of the Fujian sand particles using 3D µCT images. This system consists of an X-ray beam tub, a high-voltage generator, a sample manipulator, and a flat panel detector. The generated X-ray passes through the sample, casting the shadow image on the detector to form one projection. For high-quality µCT images, 3000 projections were taken in this study for each scan as the sample rotated 360°. The dimension sizes of the used 3D µCT images were 1400 × 1400 × 90 (width × height × depth) voxels, including 318 separate Fujian sand particles, as shown in Figure 2a. To reconstruct the 3D Fujian sand particles from the µCT images accurately, the first vision foundation model, the Segment Anything Model (SAM), was used [24]. The main components of the SAM are an image encoder, a prompt encoder, and a mask decoder, as shown in Figure 2b.

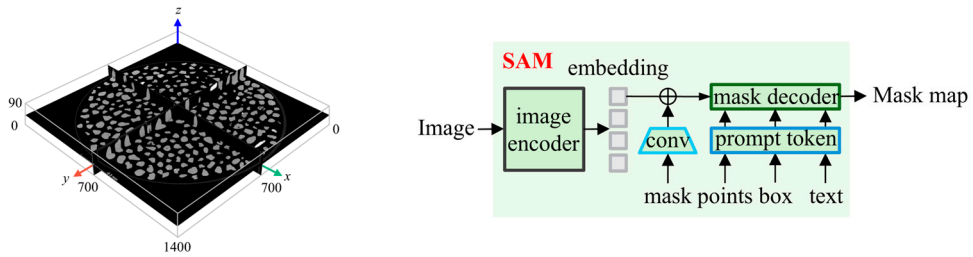

(**a**) (**b**)

Figure 2. Illustration of (**a**) 3D μCT images; (**b**) main components of SAM.

In this study, the $n \times n$ regular points were chosen as input prompts to identify all particles in the image, as shown in Figure 3a. n denotes the number of points in a row or column, taken as 32 for balancing efficiency and accuracy. All μCT slices along the z-axis were transformed into a 2D mask map by the SAM, as shown in Figure 3b. These 2D mask maps were stitched along the z-axis to form a 3D mask map. Finally, the marching cube algorithm [25] was used to convert all masks into 3D particles, as shown in Figure 3c.

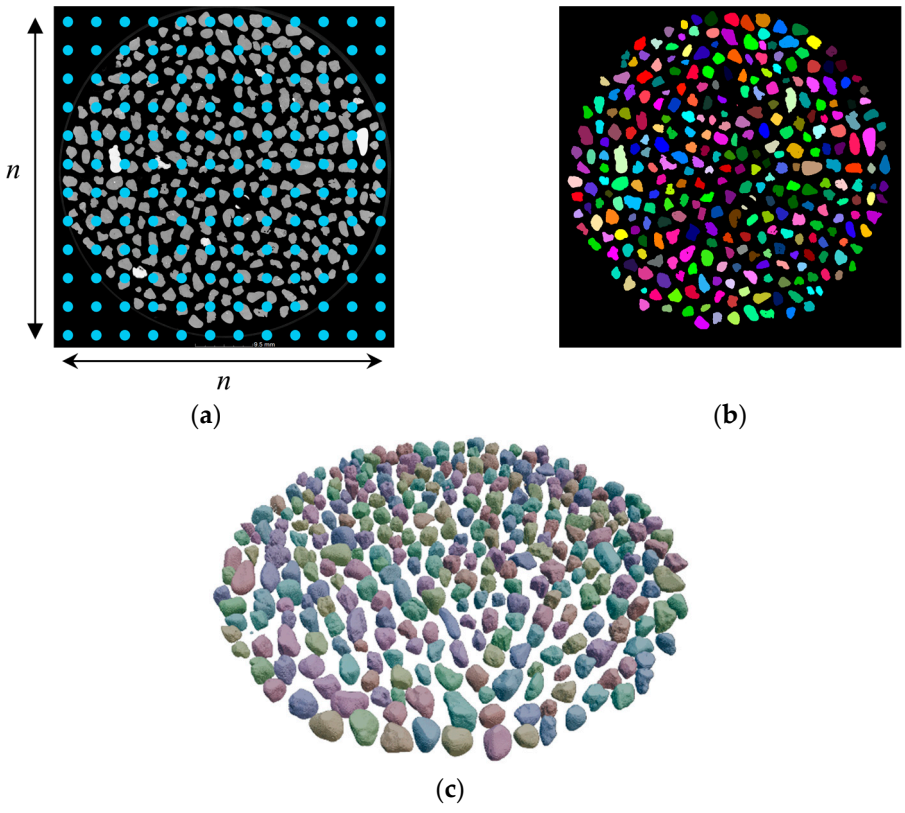

(**a**) (**b**)

(**c**)

Figure 3. Illustration of (**a**) input prompts; (**b**) 2D mask map; (**c**) 3D reconstructed particles.

2.4. Numerical Simulation

The DEM software particle flow code (PFC3D 7.0) [26] was utilized to conduct numerical single-particle crushing simulations, leveraging the reconstructed 3D particle geometries. The common bonded methods employed in the simulation of particle breakage are the bonded particle method (BPM) and the bonded block method (BBM). In the BPM, the basic cell is depicted as a rigid spherical ball, whereas the BBM employs rigid polyhedral blocks to represent the basic cell. Consequently, unexpected voids are inevitably formed between bonded spheres with only slight overlaps. On the other hand, polyhedral blocks can be modeled to ensure that adjacent faces align perfectly or slightly overlap, thereby minimizing the number of voids. Considering the limited inter-flaws and inter-voids in Fujian

sand, the simulation based on the BBM is more useful than that based on the BPM. The numerical geometry model was established based on the high-accuracy 3D reconstructed geometry in Section 2.3. The geometry used in the numerical simulation was also randomly selected from the sample for reconstruction, and the size range was the same as the tested particles. In addition, some operations on the movement and rotation of the geometry were necessary to ensure that the position and orientation during loading were consistent with the experiment. Firstly, the centroid of the geometry was translated to the origin to ensure it was centered on the loading plate. Subsequently, the geometry was rotated such that its principal axes aligned sequentially with the x, y, and z axes in descending order of their magnitudes, thereby standardizing the orientation.

A refined geometry particle modeling method for the BBM proposed by Fang et al. [27] was adopted in this study. Firstly, a specified number of balls were generated within the imported geometric shape, and then the radius of the balls gradually increased until they filled the geometric space. Furthermore, an equal number of Voronoi cells (rblocks in PFC) were generated based on the balls. Subsequently, geometry was employed again to cut the assembly of the Voronoi cells to obtain the precise numerical model. The effect of the number of cells (N_c) on the peak force decreased as the N_c increased; therefore, the N_c = 500 was adopted in this study, with limited and tolerable discrepancies of peak force and strength [28].

After the DEM geometry model was established, the linear parallel bond model, a built-in model in PFC, was applied between the blocks with the specific gap limitation, as shown in Figure 4a. The detailed behavior is described in PFC documentation [26]. This contact model provides two types of interface behavior: bonded behavior and frictional behavior. When the activated contact between the rblocks is in the bonded state, the interaction behavior is controlled by the microparameters of the parallel bond group; otherwise, the microparameters of the linear group dominate the interface behavior. If the normal and shear stress of the bonded contact exceeds the corresponding tensile and cohesive strength, the bonds of contact break and the bonded contact degenerates into a friction contact.

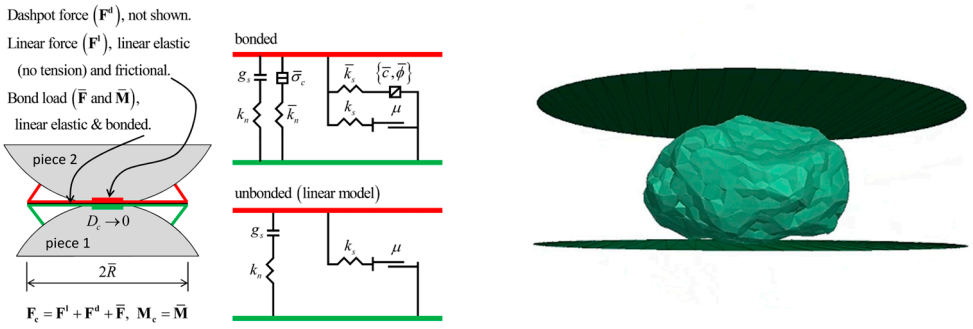

Figure 4. Illustration of (**a**) linear parallel bond model; (**b**) numerical model of the single-particle crushing test.

Two circular walls were generated at the top and bottom of the particle model, serving as the loading platens, as illustrated in Figure 4b. Considering the realistic velocity in the experiment cannot be employed in the numerical simulation due to the limited calculational efficiency, a series of numerical tests with different loading rates ranging from 0.01 m/s to 0.5 m/s were conducted to investigate the dynamic effect, as shown in Figure 5. It was observed that the peak force decreased as the loading velocity decreased and gradually stabilized. The variance in the peak force between the loading velocities of 0.4 m/s and 0.1 m/s was a mere 0.2%, which was deemed inconsequential. Therefore, a constant velocity of 0.04 m/s was employed in the following numerical model, at which the dynamic effect decreased. Moreover, to avoid dynamic stress shock in the internal rblocks, the velocity of the loading platens was gradually increased to the specified speed at the start stage.

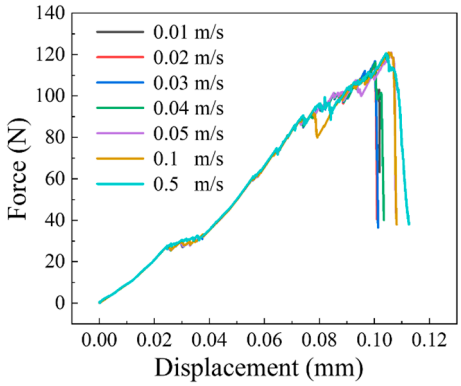

Figure 5. Force–displacement curves with different loading rates.

2.5. Shape Indexes and Fractal Dimensions

Particle morphology is generally evaluated by using shape indexes. In this study, three common shape indexes were used: the elongation index (*EI*), flatness index (*FI*), and sphericity index (*SI*). The *EI* and *FI* were used to quantify the form of the particles and are defined as follows [29]:

$$EI = \frac{b}{a} \tag{5}$$

$$FI = \frac{c}{b} \tag{6}$$

where a, b, and c are the major, intermediate, and minor principal dimensions of a particle, respectively. The *SI* is defined as the surface area of a sphere, enclosing the same volume V as the 3D object. This index is commonly used for the measuring of compactness and can be derived from the classical isoperimetric inequality and calculated as follows:

$$SI = \frac{\sqrt[3]{36\pi V^3}}{A} \tag{7}$$

where V and A denote the volume and surface area of the particle, respectively. In this study, the equivalent volume diameter d of a particle was used to quantify the particle size:

$$d = \sqrt[3]{\frac{6V}{\pi}} \tag{8}$$

The 3D particles or fragments were first converted to voxels (3D images). Then, the 3D fractal dimension F_D of the particles was calculated by using the box-counting method [30], expressed as follows:

$$F_D = \lim_{r \to 0} \frac{\log(N_r)}{\log(1/r)} \tag{9}$$

where r is the cube size, which ranges from the smallest unit in the voxel scale to 1/2 of the entire volume, and N_r is the total number of cubes containing the object of interest in the r scale. More details about the computation of the 3D fractal dimensions of particles can be found in [31]. The coefficient of determination (R^2) and mean squared error (MSE) were adopted to evaluate the fitting quality:

$$R^2 = 1 - \frac{SS_{\text{res}}}{SS_{\text{tot}}} \tag{10}$$

$$\text{MSE} = \frac{1}{n}\sum_{i=1}^{n}\left(Y_i - \hat{Y}_i\right)^2 \tag{11}$$

where SS_{res} and SS_{tot} are the sum of the squares of the residuals and the total sum of the squares, respectively, n denotes the total number, and Y_i and $\hat{Y}_i$ are the observed and predicted values, respectively.

3. Analysis of Experimental and Numerical Simulations

3.1. Experimental Results

Figure 6 presents typical force–displacement curves alongside the corresponding photographs of the representative tested particles before and after undergoing the crushing test. Due to the fine engineering properties of Fujian sand, most of the particles exhibit a smooth (result 1 in Figure 6) or slight sawtooth (result 2 in Figure 6) force–displacement curve preceding a sudden force decrease as the final catastrophic fracture. The tested particles tended to break into two to four primary fragments, occasionally accompanied by a scattering of minor fragments and some fine powder, as shown in Figure 7. This behavior aligned with the identification of the two fracture mechanisms reported by Nakata et al. [21]. During compression, localized damage at the contact points or edges led to the initial sawtooth pattern observed in the force–displacement curves and resulted in the formation of minor fragments. Subsequently, catastrophic failure occurred, causing the particle to split into two or three major fragments. These two fracture patterns are defined as asperity fracture and splitting fracture, respectively. The strength and the probability of the survival of each particle are depicted in Figure 8a and Figure 8b, respectively. The characteristic stress σ_0 in the test was 50.65 MPa, consistent with previous studies [21].

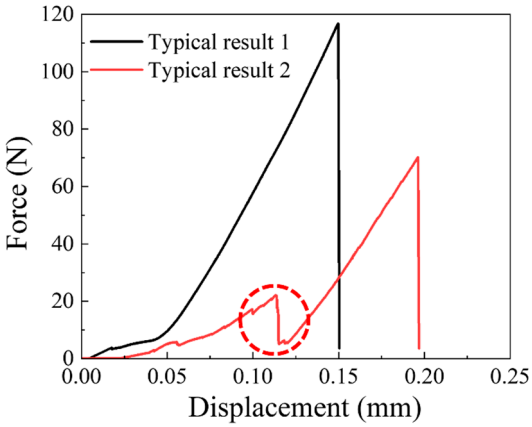

Figure 6. Typical force–displacement curves. The slight sawtooth is marked by the dotted circle.

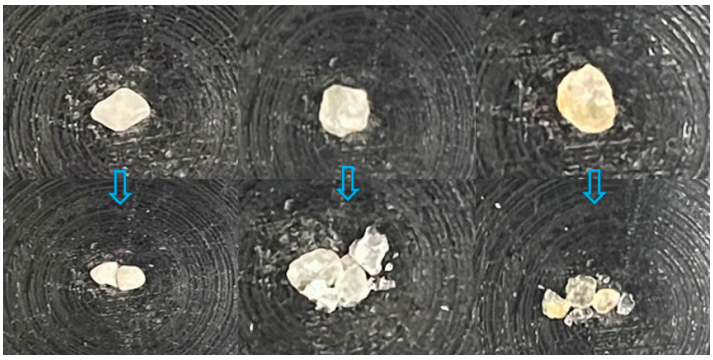

Figure 7. Representative fragmentations of sand particles.

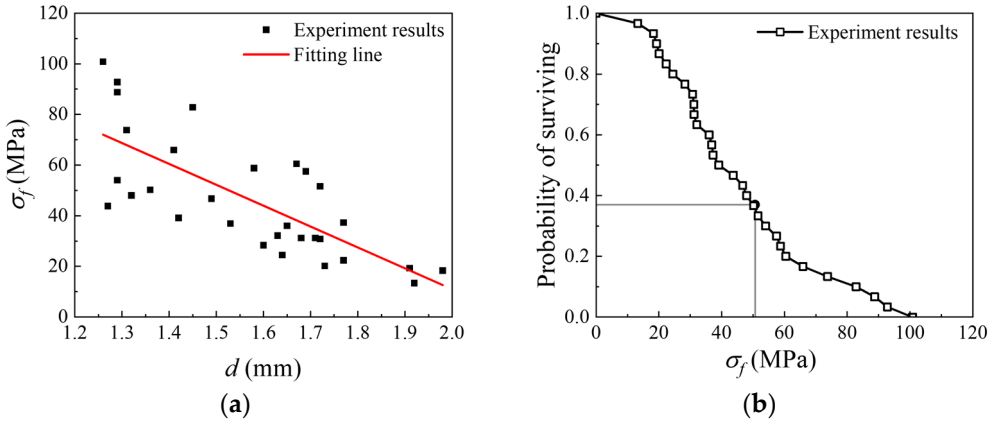

Figure 8. Experimental results: (**a**) single-particle crushing strength; (**b**) probability of survival.

3.2. Numerical Calibration

The microparameters of the contact model were calibrated by matching the characteristic strength σ_0 of the particles calculated from the results of the single-particle crushing test. After finely adjusting the microparameters of the linear parallel bond model, the distribution of the probability of surviving was similar to the experimental results as shown in Figure 9a, and the characteristic stress in the simulation was 51.38 MPa, well in agreement with the 50.65 MPa in the experiment. Furthermore, the typical force–displacement curves of the simulation results are depicted in Figure 9b, capturing the different fracture patterns illustrated in Figure 6. This correlation serves as a compelling validation of the numerical model's applicability and its capacity to accurately emulate single-particle breakage behaviors. The calibrated microparameters used in the DEM are listed in Table 1.

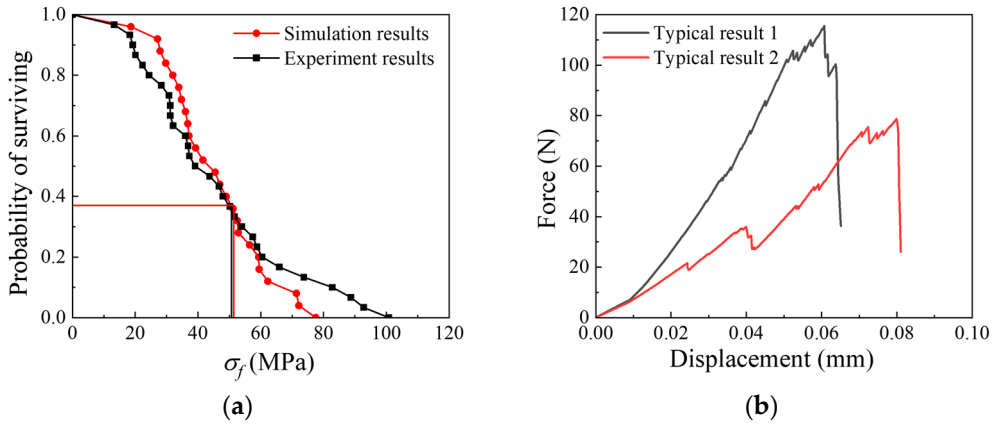

Figure 9. Calibration of numerical simulations: (**a**) distribution of the probability of surviving; (**b**) typical force–displacement curves.

It can be observed from Figure 9a that discrepancies exist between the experimental and simulated curves, particularly at their extremities, which can be attributed to two principal factors. Firstly, in the experiment, the radius of the particles was manually measured using an electronic micrometer caliper, whereas in the simulation, the radius of the particles was represented by the distance between two loading platens. Overall, the measurement radius in the simulation was smaller than that in the experiment. Secondly, the simulation did not account for flaws and incomplete homogeneity within the particles. As a result, the variation in strength observed in the simulations was less pronounced than that in the experiments. This disparity is reflected in the Weibull modulus (m) values, with an experimentally determined value of m = 2.21 compared to a value of m = 3.15 obtained from the simulations.

Table 1. Microparameters used in DEM simulation.

Microscale Parameters	Value
Particle density (kg/m^3)	2650
Damping	0.5
Frictional coefficient	0.5
Bond effective modulus (GPa)	1.9
Bond normal to shear stiffness ratio	2.5
Bond tensile strength (MPa)	29
Bond cohesive strength (MPa)	28.5
Rblock effective modulus (GPa)	1.9
Rblock normal to shear stiffness ratio	2.5
Wall elastic modulus (GPa)	1.9
Wall normal to shear stiffness ratio	1

Regarding the fragmentations produced by the catastrophic failure of the particle, as shown in Figure 10, the numerical model yielded a primary fragment count ranging from 2 to 4 pieces, thereby demonstrating a close concurrence with the experimental observations. Furthermore, within the contact zone, the isolated block marked in navy blue represents the abrasion and asperity fracture of the particle.

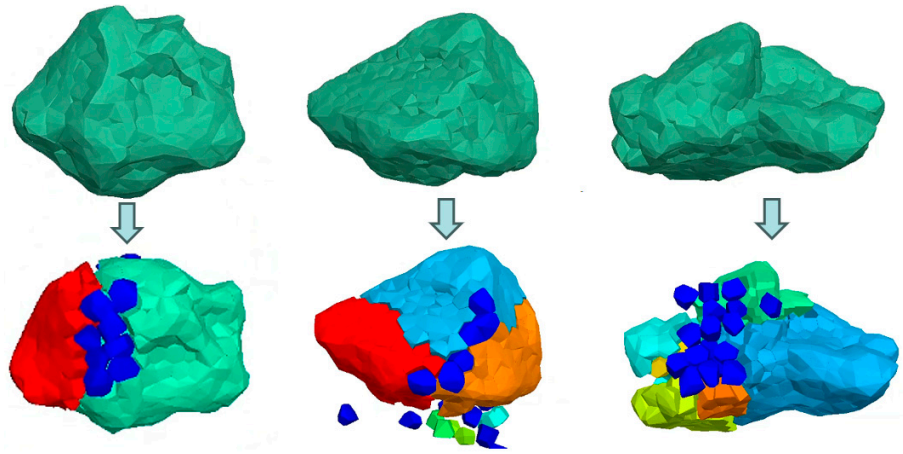

Figure 10. Numerical results of particles before and after breakage. Each color represents a particle.

4. Relations Between Fractal Dimensions, Particle Size, Crushing Strength, and Morphology

The application of fractal theory to investigate the relationship between 3D fractal dimensions, particle size, particle crushing strength, and morphology holds significant practical implications. Understanding these relationships can lead to improved material performance in various industries. Furthermore, by establishing a quantitative link between fractal dimensions and mechanical properties, engineers can design materials with tailored characteristics, optimizing them for specific applications.

4.1. Relations Between Fractal Dimensions and Particle Size

The statistical results of the particle size d before and after the breakage are presented in Figure 11a and Figure 11b, respectively. It is clear that particle sizes ranged from 1.2 mm to 1.8 mm before the single-particle breakage. The number of particles with a size between 1.4 mm and 1.5 mm was the highest. The dominant particle size ranged from 0.2 mm to 0.4 mm after the breakage, consistent with the experimental results. Small-size fragments were mostly observed in single-particle breakage fragments. Notably, the fine fragments or powder-like particles within the size range of 0 mm to 0.2 mm were excluded from the statistical analysis, as they were not encompassed within the defined size range for the blocks under consideration. Therefore, the count in this range was zero.

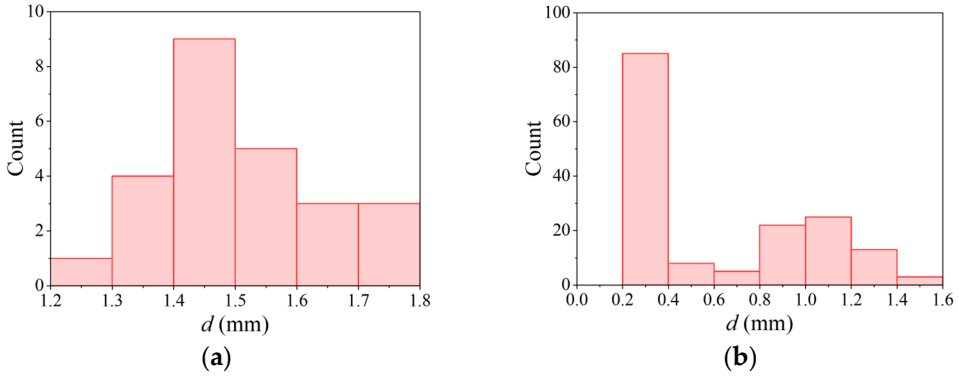

Figure 11. Statistical results of particle size *d*: (**a**) before breakage; (**b**) after breakage.

The correlation between the 3D fractal dimension of the particles and the particle size before and after the particle breakage are presented in Figure 12a and Figure 12b, respectively. It can be seen that the particle size decreased while the fractal dimension increased. The particle size before the breakage and the 3D fractal dimension can be fitted by a straight line with R^2 = 0.625. The unsatisfactory R^2 value may be attributed to the insufficient number of simulations. The fitting results could be improved by incorporating a greater number of simulations. Moreover, the accuracy of the reconstructed 3D models also plays a significant role. Inaccurate surface details in the 3D model can introduce noise, which in turn may lower the R^2 value. Interestingly, the relation between the particle size after the breakage and the 3D fractal dimension can be interpreted by an exponential function with a high R^2 = 0.931. These results suggest that the fractal dimension after particle breakage is significantly affected by the particle size. The sizes of many small fragments are similar, but the individual fractal dimensions exhibit significant variation. A possible explanation is that smaller particle fragments are more likely to be irregular in shape, resulting in varying fractal dimensions. The difference in the relation between the particle size distribution and 3D fractal dimension before and after breakage can be used as an indicator for identifying the breakage degree.

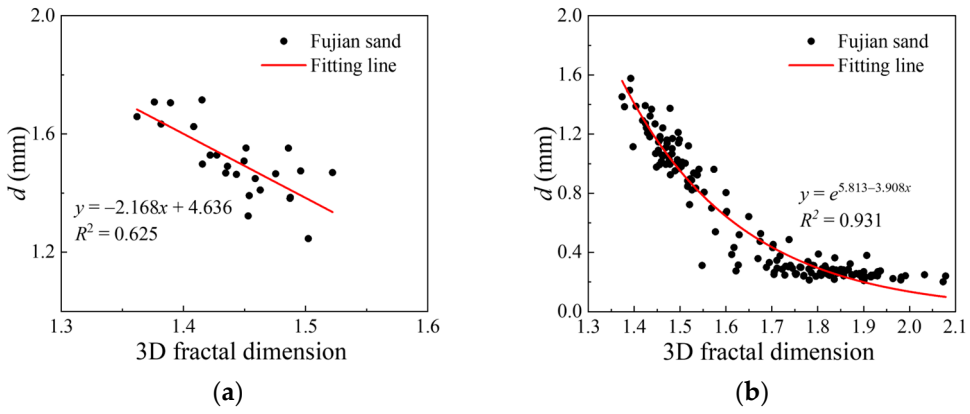

Figure 12. Relations between 3D fractal dimension and particle size: (**a**) before breakage; (**b**) after breakage.

The relation between the particle crushing strength σ_f and 3D fractal dimension is presented in Figure 13. The result indicates that the particle crushing strength σ_f increased with the 3D fractal dimension. These scatter points can be fitted by a straight line with MSE = 73.091. It can be concluded that the particles with a higher 3D fractal dimension resulted in higher particle crushing strength. This provides an auxiliary to predict the particle crushing strength based on the 3D fractal dimension. However, the data used in this study are insufficient to obtain an accurate relationship between the 3D fractal dimension and particle crushing strength. Nevertheless, a more complicated model could

be established if more experimental data are provided, guaranteeing a better understanding of the relationship between the 3D fractal dimension and particle crushing strength. More importantly, in practice, the crushing strength of particles can be quickly estimated by measuring their 3D fractal dimension, and the macroscopic mechanical properties of materials can be thereby inferred. This can save a lot of experimental time and costs and optimize material selection and design processes.

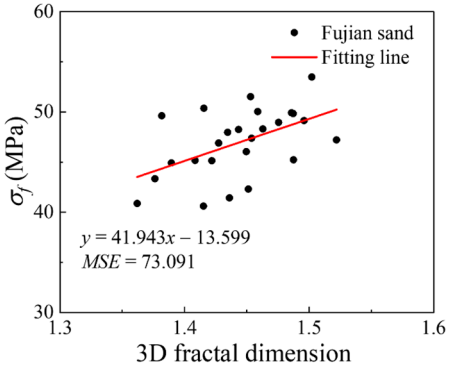

Figure 13. Relations between 3D fractal dimension and particle crushing strength.

4.2. Relations Between Fractal Dimensions and Morphology

The correlation between the 3D fractal dimension of the particles before the breakage and particle shape indexes (*EI*, *FI*, and *SI*) of granular materials are shown in Figure 14a, Figure 14b, and Figure 14c, respectively. It can be observed that the *EI* and *SI* increased as the 3D fractal dimension increased. However, the shape index *FI* decreased as the 3D fractal dimension increased. This is an expected result since higher *FI* values indicate higher particle shape irregularities, and it is well known that increasing particle irregularities increase fractal dimension [32]. The *MSE* value of the fitting line for the *SI* is the lowest one, suggesting that the *SI* is more appropriate to be used for examining the 3D fractal dimension of intact particles indirectly.

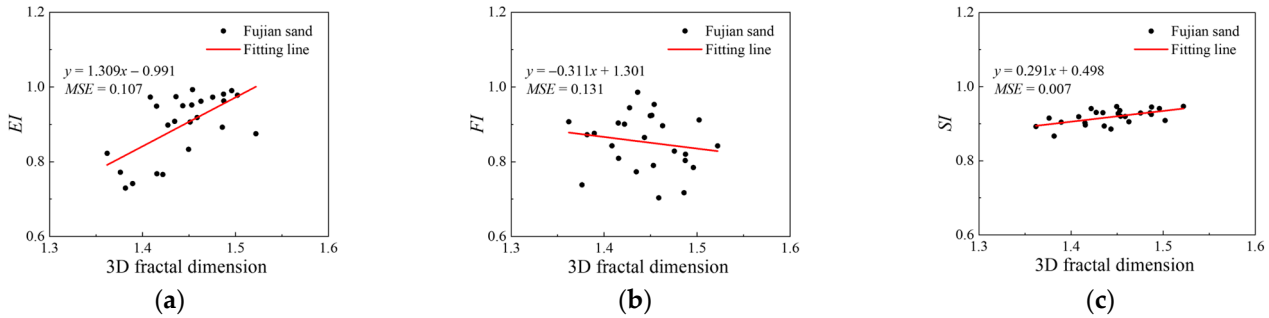

Figure 14. Relations between 3D fractal dimension and particle shape indexes before breakage: (**a**) *EI*; (**b**) *FI*; (**c**) *SI*.

Similarly, the correlation between the 3D fractal dimension of the particles after the breakage and particle shape indexes (*EI*, *FI*, and *SI*) of granular materials are shown in Figure 15a, Figure 15b, and Figure 15c, respectively. Conversely, the shape indexes *EI* and *SI* decreased as the 3D fractal dimension increased, while the *FI* increased as the 3D fractal dimension increased. The relation between the 3D fractal dimension and shape indexes is completely different before and after breakage. This result may be related to the change in the particle size distribution, where the irregular small fragments dominate the fragmented particles. The quick increase in the small irregular fragments alters the relationship between the 3D fractal dimension and shape indexes. The relationship between the 3D fractal dimension and shape indexes is extremely different before and after breakage.

This result suggests that the 3D fractal dimension can also be a good indicator for describing particle morphology, thus predicting the mechanical behaviors of particles.

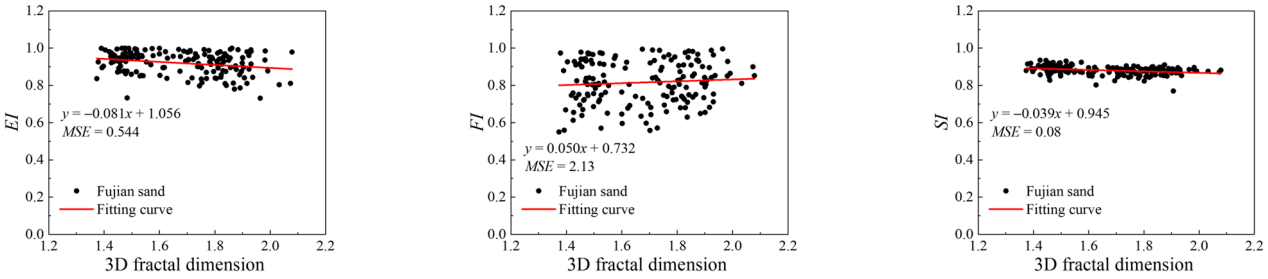

Figure 15. Relations between 3D fractal dimension and particle shape indexes after breakage: (**a**) *EI*; (**b**) *FI*; (**c**) *SI*.

5. Conclusions

A systematic framework for investigating single-particle breakage from experiments to numerical simulations based on three-dimensional (3D) images was developed in this study. A novel 3D particle reconstruction method utilizing the vision foundation model was proposed and demonstrated to be effective. This approach provides a novel alternative for reconstructing particles from 3D images. The reconstructed 3D accurate particles were calibrated and modeled by the discrete element method (DEM) with the bonded block method (BBM), based on one-to-one mapping single-particle loading tests. The results showed that the calibrated numerical simulations were sufficient to mimic the mechanical behavior of the single-particle breakage. The numerical simulations for the single-particle loading tests were performed using calibrated parameters. Moreover, fractal theory was used to investigate the relationship between the 3D fractal dimensions and particle size, particle crushing strength, and morphology. The relationship between the 3D fractal dimension and shape indexes changed significantly before and after the breakage. The results indicate that the particle size decreased as the fractal dimension increased. The trend of the particles before the crushing can be fitted with a straight line, while the trend of the particles after the crushing can be fitted with an exponential function. The particles with a higher 3D fractal dimension had a higher particle crushing strength. After the particle breakage, the *EI* and *FI* exhibited a slight decrease as the 3D fractal dimension increased. Conversely, the *SI* decreased as the 3D fractal dimension increased. The 3D fractal dimension is a good indicator for describing particle morphology and particle crushing strength. A more comprehensive conclusion can be found if more experimental data are available.

The proposed framework achieved a robust and accurate simulation for single-particle breakage, providing an auxiliary approach for investigating particle breakage from experiments to numerical simulations based on fractal theory. However, particle morphology could be accurately captured but did not consider the scenarios in which particles are connected. The influence of multi-point contact on single-particle breakage was also not revealed and will be investigated in future work. Moreover, a model comparing particle shape, crushing strength, 3D fractal dimension, and macroscopic mechanical properties can be developed by the physical-informed neural network (PINN) to obtain more accurate numerical simulation tools and provide reliable prediction results for engineering practice.

Author Contributions: Conceptualization, R.L. and X.G.; methodology, S.-H.H.; software, X.G.; experiment, D.R.; formal analysis, R.L.; data curation, S.-H.H.; writing—original draft preparation, R.L. and X.G.; writing—review and editing, S.-H.H.; supervision, S.-H.H. and Z.D.; project administration, S.-H.H.; funding acquisition, S.-H.H. and Z.D. All authors have read and agreed to the published version of the manuscript.

Funding: This research was financially supported by the National Natural Science Foundation of China under Grant No. 52178400.

Data Availability Statement: Data will be available upon reasonable request.

Conflicts of Interest: The authors declare no conflicts of interest.

References

1. Yu, F. Particle breakage in granular soils: A review. *Part. Sci. Technol.* **2021**, *39*, 91–100. [CrossRef]
2. Wang, P.; Xu, C.; Yin, Z.-Y.; Song, S.; Xu, C.; Dai, S. A DEM-based Generic Modeling Framework for Hydrate-Bearing Sediments. *Comput. Geotech.* **2024**, *171*, 106287. [CrossRef]
3. Tavares, L.M. Review and further validation of a practical single-particle breakage model. *KONA Powder Part. J.* **2022**, *39*, 62–83. [CrossRef]
4. Tavares, L.M. Chapter 1 Breakage of Single Particles: Quasi-Static. In *Handbook of Powder Technology*; Elsevier: Amsterdam, The Netherlands, 2007; pp. 3–68. [CrossRef]
5. Tavares, L.M. Energy absorbed in breakage of single particles in drop weight testing. *Miner. Eng.* **1999**, *12*, 43–50. [CrossRef]
6. Salman, A.D.; Biggs, C.A.; Fu, J.; Angyal, I.; Szabo, M.; Hounslow, M.J. An experimental investigation of particle fragmentation using single particle impact studies. *Powder Technol.* **2002**, *128*, 36–46. [CrossRef]
7. Rumpf, H. Physical aspects of comminution and new formulation of a law of comminution. *Powder Technol.* **1973**, *7*, 145–159. [CrossRef]
8. Saeidi, F.; Yahyaei, M.; Powell, M.; Tavares, L.M. Investigating the effect of applied strain rate in a single breakage event. *Miner. Eng.* **2017**, *100*, 211–222. [CrossRef]
9. Zhang, T.; Yang, W.; Zhang, C.; Hu, C. Particle Breakage Effect on Compression Behavior of Realistic Granular Assembly. *Int. J. Geomech.* **2021**, *21*, 04021105. [CrossRef]
10. Kh, A.B.; Mirghasemi, A.A.; Mohammadi, S. Numerical simulation of particle breakage of angular particles using combined DEM and FEM. *Powder Technol.* **2011**, *205*, 15–29.
11. Zhang, C.; Ren, Z.; Hao, D.; Zhang, T. Numerical Simulation of Particle Size Influence on the Breakage Mechanism of Broken Coal. *Arab. J. Sci. Eng.* **2020**, *45*, 9171–9185. [CrossRef]
12. Li, H.; McDowell, G.R.; Lowndes, I. Discrete-element modelling of rock breakage using dense random packing agglomerates. *Géotechnique Lett.* **2013**, *3*, 98–102. [CrossRef]
13. Potyondy, D.O.; Cundall, P.A. A bonded-particle model for rock. *Int. J. Rock Mech. Min. Sci.* **2004**, *41*, 1329–1364. [CrossRef]
14. Barrios, G.K.P.; Jiménez-Herrera, N.; Tavares, L.M. Simulation of particle bed breakage by slow compression and impact using a DEM particle replacement model. *Adv. Powder Technol.* **2020**, *31*, 2749–2758. [CrossRef]
15. Delaney, G.W.; Morrison, R.D.; Sinnott, M.D.; Cummins, S.; Cleary, P.W. DEM modelling of non-spherical particle breakage and flow in an industrial scale cone crusher. *Miner. Eng.* **2015**, *74*, 112–122. [CrossRef]
16. Washino, K.; Chan, E.L.; Nishida, Y.; Tsuji, T. Coarse grained DEM simulation of non-spherical and poly-dispersed particles using Scaled-Up Particle (SUP) model. *Powder Technol.* **2023**, *426*, 118676. [CrossRef]
17. Pan, J.; Pinzón, G.; Wang, R.; Andò, E.; Viggiani, G.; Zhang, J.-M. Lessons learned from matching 3D DEM and experiments at macro, meso and fabric scales for triaxial compression tests on lentils. *J. Mech. Phys. Solids* **2024**, *183*, 105494. [CrossRef]
18. Scholtès, L.; Donzé, F.-V. A DEM model for soft and hard rocks: Role of grain interlocking on strength. *J. Mech. Phys. Solids* **2013**, *61*, 352–369. [CrossRef]
19. Brown, G.J.; Miles, N.J.; Jones, T.F. A fractal description of the progeny of single impact single particle breakage. *Miner. Eng.* **1996**, *9*, 715–726. [CrossRef]
20. Arasan, S.; Akbulut, S.; Hasiloglu, A.S. The relationship between the fractal dimension and shape properties of particles. *KSCE J. Civ. Eng.* **2011**, *15*, 1219–1225. [CrossRef]
21. Nakata, A.F.L.; Hyde, M.; Hyodo, H.; Murata. A probabilistic approach to sand particle crushing in the triaxial test. *Géotechnique* **1999**, *49*, 567–583. [CrossRef]
22. Jaeger, J.C. Failure of rocks under tensile conditions. *Int. J. Rock Mech. Min. Sci. Geomech. Abstr.* **1967**, *4*, 219–227. [CrossRef]
23. McDowell, G.R. Statistics of soil particle strength. *Géotechnique* **2001**, *51*, 897–900. [CrossRef]
24. Kirillov, A.; Mintun, E.; Ravi, N.; Mao, H.; Rolland, C.; Gustafson, L.; Xiao, T.; Whitehead, S.; Berg, A.C.; Lo, W.-Y.; et al. Segment Anything. *arXiv* **2023**. [CrossRef]
25. Lorensen, W.E.; Cline, H.E. Marching cubes: A high resolution 3D surface construction algorithm. *SIGGRAPH Comput. Graph.* **1987**, *21*, 163–169. [CrossRef]
26. Itasca, User's Manual for pfc3d. 2019. Available online: https://docs.itascacg.com/pfc600/contents.html (accessed on 19 January 2024).
27. Fang, C.; Gong, J.; Nie, Z.; Li, B.; Li, X. DEM study on the microscale and macroscale shear behaviours of granular materials with breakable and irregularly shaped particles. *Comput. Geotech.* **2021**, *137*, 104271. [CrossRef]
28. Fang, C.; Nie, Z.; Gong, J.; Li, B.; Hu, W.; Mohammed, A. Discrete element simulation of effects of multicontact loading on single particle crushing. *Particuology* **2022**, *69*, 49–60. [CrossRef]

29. Zingg, T. Beitrag zur Schotteranalyse. Ph.D. Thesis, ETH Zurich, Zurich, Switzerland, 1935. Available online: https://www.research-collection.ethz.ch/bitstream/handle/20.500.11850/135183/1/eth-21472-01.pdf (accessed on 19 January 2024).
30. So, G.-B.; So, H.-R.; Jin, G.-G. Enhancement of the box-counting algorithm for fractal dimension estimation. *Pattern Recognit. Lett.* **2017**, *98*, 53–58. [CrossRef]
31. Li, J.; Du, Q.; Sun, C. An improved box-counting method for image fractal dimension estimation. *Pattern Recognit.* **2009**, *42*, 2460–2469. [CrossRef]
32. Kolay, E.; Kayabali, K. Investigation of the effect of aggregate shape and surface roughness on the slake durability index using the fractal dimension approach. *Eng. Geol.* **2006**, *86*, 271–284. [CrossRef]